Nuclear Science and Techniques (2026) 37:8
https://doi.org/10.1007/s41365-025-01816-y

A 32-channel charge-sensitive amplifier for delay-line readout of parallel plate avalanche counter array

Yue-Zhao Zhang[1,2] · Peng Ma[1] · Zhuang-Yu Lin[1] · Zhen-Fei Tan[3] · Xing-Chi Han[1] · Chen Liu[1,2] · Shuo Wang[1,2] · Da-Peng Sun[1,2] · Zhi-Quan Li[4] · En-Hong Wang[1] · Shou-Yu Wang[1,2]

Received: 26 January 2025 / Revised: 2 June 2025 / Accepted: 10 June 2025 / Published online: 6 December 2025

Abstract
A 32-channel charge-sensitive amplifier (CSA) is designed for fast timing in the delay-line readout of a parallel plate avalanche counter (PPAC) array. It is realized on a PCB with operational amplifiers and other discrete components. Each channel consists of an integrator, a pole-zero cancellation net, and a linear amplification stage, which can be adapted to accommodate either positive or negative input signals. The RMS equivalent input noise charges are 3.3 fC, the conversion gains are approximately ± 2 mV/fC, and the intrinsic time resolution reaches 32 ps. In the prototype PPAC application, the CSA performs as well as the commercial FTA820A amplifier, providing a position resolution as good as 0.17 mm, and exhibiting reliable stability during several hours of continuous data acquisition.

Keywords Charge-sensitive amplifier · Fast timing · Parallel plate avalanche counter · Delay-line · Discrete components

1 Introduction

Radiation detectors are widely used in heavy-ion collision experiments to study nuclear structures and reactions. The kinematics of the secondary protons, neutrons, and ions can be effectively measured using detectors. The coincident measurement of secondary particles and particle-photon coincidence provide insights into the collision dynamics, energy level structure, or other internal states of the participants. Low-pressure parallel plate avalanche counters (PPACs) [1–3], semiconductor silicon detectors [4], and solid scintillation detectors [5] are among the most commonly used detectors in the above-mentioned situations. PPAC is better suited than scintillation detectors for fast timing and position measurement. Subnanosecond and submillimeter resolutions can be achieved simultaneously on a sensitive area of several hundred cm^2. PPAC detectors are more radiation-tolerant and cost-efficient than silicon detectors.

To study Coulomb excitation of atomic nuclei [6], we developed a PPAC array. It consists of 20 PPAC units that can cover almost a 4π solid angle around a solid target, similar to the CHICO2 array [2]. During the collision between the projectile and target nuclei, both may become excited through Coulomb interactions. Soon after excitation, gamma rays were emitted during deexcitation. The PPAC array detects the two-dimensional positions and the flight time difference of the recoil and scattered nuclei; thus, nucleus identification and Doppler correction of the gamma-ray energy can be performed [7]. Each PPAC unit is capable of sub-nanosecond time resolution, which is obtained via the signal from the membrane electrode, and submillimeter position resolution, enabled by the four signals from two perpendicular delay lines. The delay-line and membrane

This work was supported by the National Natural Science Foundation of China (Nos. U2167202, 12225504, 12005276), the Natural Science Foundation of Shandong Province (No. ZR2024QA172), and the Fundamental Research Funds of Shandong University.

✉ Shou-Yu Wang
sywang@sdu.edu.cn

[1] Shandong Provincial Key Laboratory of Nuclear Science, Nuclear Energy Technology and Comprehensive Utilization, Shandong University, Shandong 250061 Weihai, China

[2] Weihai Research Institute of Industrial Technology of Shandong University, Weihai 264209, China

[3] School of Space Science and Technology, Shandong University, Weihai 264209, China

[4] SDU-ANU Joint Science College, Shandong University, Weihai 264209, China

signals had opposite polarities. They are immediately processed by the preamplifiers, which output negative voltage pulses to the discriminators, that is, both positive and negative detector current pulses should be converted to negative voltage pulses. Because each PPAC unit requires five readout channels, a total of 100 channels are required.

The performance of the preamplifier directly affected the resolution of the detector system. Various customized preamplifiers have been developed to adapt to different detectors. The integration schemes of multichannel preamplifiers can be roughly classified into three types. Integration of semiconductor pixel application-specific integrated circuits (ASICs), such as Timepix [8], MIMOSA [9], ALPIDE [10], Taichupix [11], Jadepix [12], Topmetal [13], Nupix [14], and IMPix [15]. The preamplifier, together with certain electronic stages, is photoetched adjacent to the detector sensor in the same bulk or connected to the sensor via eutectic solder bumps. The pixel size is several tens to hundreds of micrometers, which offers micrometer position resolution. These pixel ASICs find applications as vertex or tracking detectors in large-scale collider experiments, where thousands or more high-density electronics are required [10, 11], or in places of ultrahigh position resolution, such as beam telescopes [16] and spectroscopic X-ray imaging [17]. The second is chip-level integration. Encapsulation of several to over hundred channels of front-end electronics (FEE), including the preamplifier stage, has been achieved on a semiconductor chip. Typical examples include SAMPA [18], NINO [19], AGET [20], AFTER [21], TOFPET [22], and PADI [23]. The connection between the detector readout electrodes and FEE is established using transmission lines, usually on a printed circuit board (PCB). Separation of the FEE from the detector limits the detector patch size, as encountered in pixel ASICs, whereas chip-level integration still guarantees a high circuit density. Hence, this scheme is widely adopted in large-area detectors and other applications where high-density readout electronics are pursued, for example, the time projection chamber (TPC), muon chamber, and time of flight (ToF) detectors in the ALICE experiment [18, 24, 25], silicon tracker and BGO calorimeter on the DAMPE satellite [26, 27], Compton telescope for dose monitoring in hadron therapy [28], and ToF detectors in positron emission tomography (PET) [29]. Third, there is board-level integration. Typically, tens of channels can be realized on a single PCB. Each channel is constructed with discrete elements, including operational amplifiers (OPAs), resistors, and capacitors. This solution is usually adopted in situations where hundreds of channels are required and the board-level circuit density is acceptable. Compared to the chip-level realization, the dynamic range and circuit logic can be adjusted more conveniently and economically to meet various requirements, by selecting adequate elements from the vast commercial market. Typical applications can be found in the SPA02-16 and SPA03-16 preamplifier modules for silicon detector array [30], the multi-purpose TPC at CSNS Back-n [31], the NEXT experiment in search of $0\nu\beta\beta$ decay [32, 33], the scintillation detector array designed for PET [34], the CZT-based gamma-ray spectrometer [35], and the ITER radial X-ray camera [36], etc.

In this study, a third scheme was adopted. A versatile 32-channel charge-sensitive amplifier (CSA) is designed for the PPAC array under development. Section 2 describes the schematic and PCB design of the amplifier, Sect. 3 presents the performance calibrations, Sect. 4 shows the test results for application to a prototype PPAC, and Sect. 5 concludes this work.

2 Schematic circuit diagram and PCB design

The PPAC array model under development is illustrated in Fig. 1. Twenty identical trapezoidal PPACs were arranged inside a ∅50 cm spherical chamber, covering nearly the full 4π solid angle. In physical experiments, energetically charged particles are emitted from a solid target at the chamber center and detected by the PPACs. The detectors measured the particle emission directions and the striking time difference between them.

The particle emission polar and azimuthal angles were deduced from the particle hitting position on the detector, which was read out using a pixel-strip delay-line anode. In Fig. 1b, all the other structures are removed, except for the top layer of the anode PCB, gas area, and particle entrance membrane. Trapezoidal metallic pixels of equal altitude are distributed on the top layer of the anode PCB facing the particle entrance membrane. Readout strips are formed by connecting every other pixel in one of the two orthogonal directions, denoted by θ and φ. Pixel connections were made between the inner layers of the anode PCB. Furthermore, the strips were connected using inductors and capacitors to implement a delay-line readout scheme. In the θ direction, the detector position resolution should be better than 3 mm, corresponding to a maximum polar angle of 0.93°. In the φ direction, the detector position resolution should be better than 1.3 mm, corresponding to a maximum azimuthal angle of 1.5°. The particle impact time was determined from the cathode membrane. Considering [1] as a reference, the time resolution should be better than 350 ps.

The characteristic fast responses of the typical PPACs are listed in Table 1. A total of 10^6 to 10^7 electron-ion pairs can be generated in avalanche multiplication [37, 38]. However, only 10% of all electrons contribute to the fast signal [39, 40]. The rise time is normally 5–10 ns [37–41], which is defined as the time required for the signal to rise from 10% to 90% of its amplitude. The full width was approximately 15 ns [37, 40], which is the duration between the signal

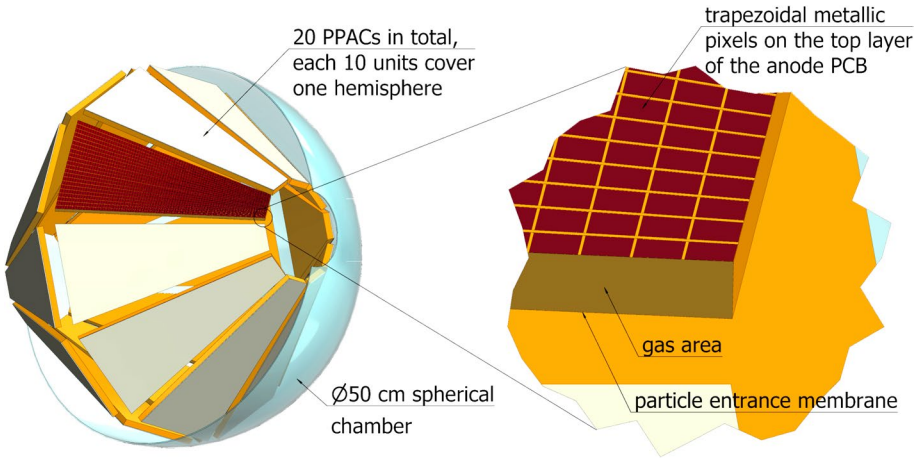

Fig. 1 (Color online) **a** Sketch of the PPAC array. There are 20 identical trapezoidal PPACs arranged inside a Ø50 cm spherical chamber. Each set of ten covered one hemisphere. **b** Corner of a PPAC unit showing the preliminary design of the readout pixel pattern. All other structures were removed, except for the top layer of the anode PCB, the gas area, and the particle entrance membrane. The symbols θ and φ denote two orthogonal directions parallel to the detector surface

Table 1 Typical response of PPAC detectors

Current Rise Time[1]	Current Width[2]	Current Maximum[3]	Total Avalanche Electrons
6 ns [39] 8 ns [37][4] 10 ns [40] 5 ns [41]	20 ns [37][4] 15 ns [40]	several μA	$10^6 \sim 10^7$ [37][5] 10^6 [38][5]

[1] Signal rise time is defined as the time it takes for the signal to rise from 10% to 90% of its amplitude

[2] Signal width is the duration between the signal rising past 10% of its amplitude and subsequently falling below 10% of its amplitude

[3] Estimation based on the shape and total charge in the fast current pulse induced by electrons

[4] Before the launch of the space-charge effect

[5] Only ∼ 10% of all the electrons induce the fast pulse [39, 40], i.e., in the order of 10^5

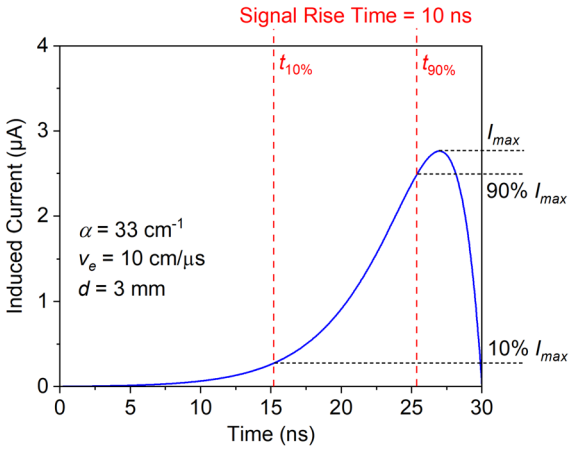

Fig. 2 A calculated fast electric current profile induced on the anode by electrons moving across a 3-mm-thick PPAC. $\alpha = 33\ \mathrm{cm}^{-1}$ is the first Townsend coefficient of the filling gas, $v_e = 10\ \mathrm{cm/\mu s}$ is the electron drift velocity, and $d = 3$ mm is the distance between the anode and cathode electrodes. (Reproduced from [40]. The units of the Y-axis and α have been corrected.)

rising past 10% of its amplitude and subsequently falling below 10% of its amplitude. Accordingly, the maximum current was estimated as several μA. The calculated fast electric current profile induced on the anode by electrons moving across a 3-mm-thick PPAC is shown in Fig. 2 [40]. The preamplifier is designed to convert the PPAC output charge to a voltage pulse of several hundred millivolts in amplitude. The width of the voltage pulse was set to the same order as that of the original current pulse width, allowing for high counting rates.

2.1 Schematic design

Each CSA channel is composed of two stages of OPA circuit. The first stage was the charge integrator (Qint). The second is a non-inverting amplification (NinvAmp) or inverting amplification (InvAmp) stage designed for different detector response polarities. Figure 3 shows schematic diagrams, that is, (a) Qint + NinvAmp and (b) Qint + InvAmp. The Qint input was AC-coupled to the detector electrode via a single-ended transmission line of 50 Ω. To control the output noise, the Qint stage was used in conjunction with a pole-zero cancellation (PZC) net. OPA657 [42] and OPA847 [43] produced by the Texas Instruments Incorporated Company were adopted in the first and second amplifier stages, respectively. Both feature a very low input voltage noise density, whereas the JFET-input stage endows OPA657 with a much lower input current noise density and input bias current. Hence, using OPA657 in the first stage provides lower noise and higher direct-current (DC) precision at the output.

The signal-to-noise ratio (SNR) of the final output is principally determined by the SNR of the Qint output. The feedback capacitor $C_{\mathrm{f1}}^{\mathrm{int}} = 5$ pF and feedback resistor $R_{\mathrm{f1}}^{\mathrm{int}} = 200$ kΩ were chosen as a balance between the noise level and the conversion gain. The time constant

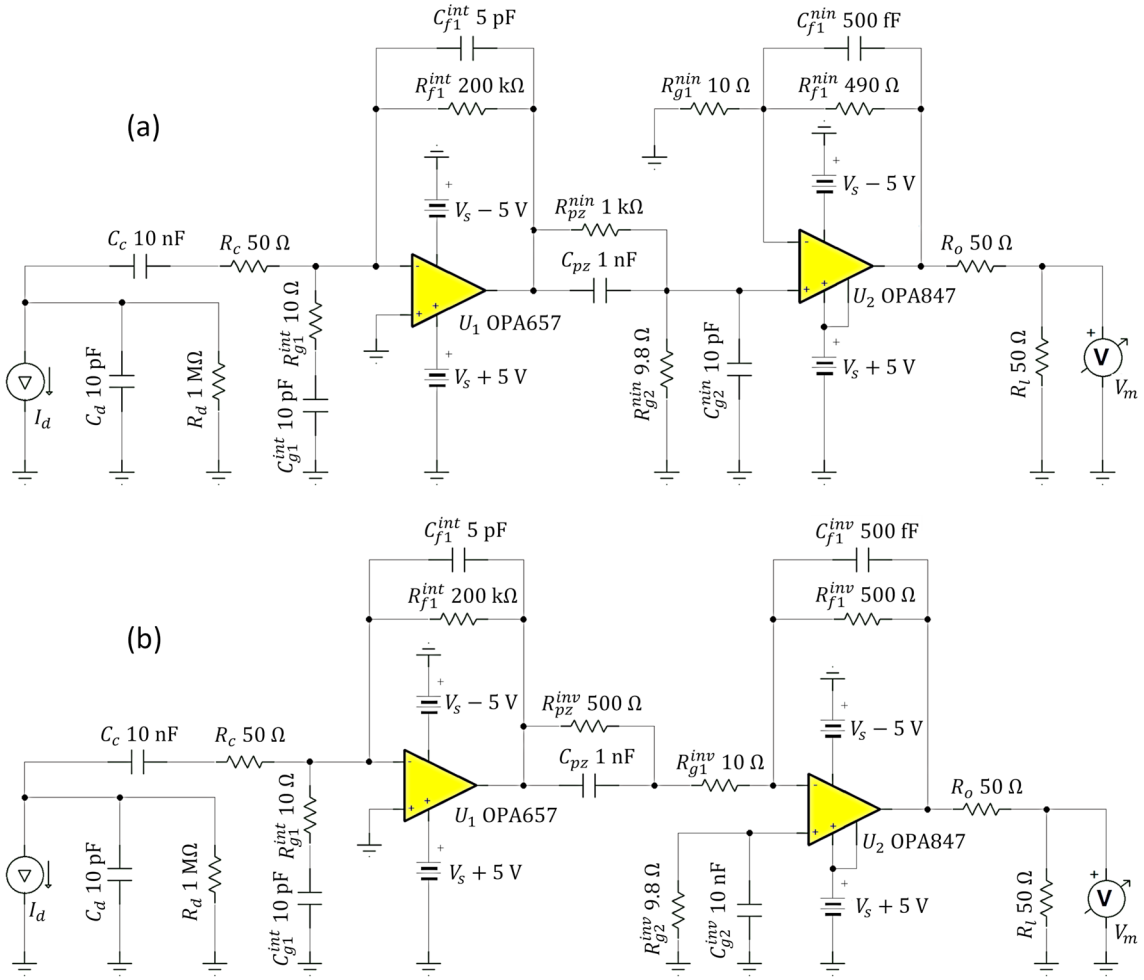

Fig. 3 Schematic diagrams of the CSAs. **a** Qint + NinvAmp. **b** Qint+ InvAmp. A PZC net was inserted between the two OPA circuits in each CSA. The components before the capacitor C_c simulate the detector response. R_l is the load resistor

$\tau_{int} = R_{f1}^{int} C_{f1}^{int} = 1$ μs. To stabilize the Qint circuit, the resistor $R_{g1}^{int} = 10$ Ω in series with the capacitor $C_{g1}^{int} = 10$ pF was installed for input lag compensation. The coupling capacitor C_c was set to 10 nF with a self-resonant frequency close to the input signal bandwidth. The resistor $R_c = 50$ Ω is the termination resistor for terminal matching of the 50 Ω input transmission line.

In the InvAmp stage, the feedback resistors are $R_{f1}^{inv} = 500$ Ω and $R_{f1}^{nin} = 490$ Ω. Resistors R_{g1}^{inv} and R_{g1}^{nin} are fixed at 10 Ω. The capacitors C_{f1}^{inv} and C_{f1}^{nin}, together with the parasitic capacitance in parallel with them (approximately 0.1 pF), function as feedback lead compensation to stabilize the circuit operation. After fine adjustment, $C_{f1}^{inv} = C_{f1}^{nin} = 0.5$ pF was installed. The pull-down resistors $R_{g2}^{inv} = R_{f1}^{inv} \| R_{g1}^{inv}$ and $R_{g2}^{nin} = R_{f1}^{nin} \| R_{g1}^{nin}$ at the non-inverting input of the OPA847 chips suppress the output DC error caused by the input bias current. The capacitors $C_{g2}^{inv} = 10$ nF and $C_{g2}^{nin} = 10$ pF are parallel to R_{g2}^{inv} and R_{g2}^{nin}, respectively. These two capacitors minimize the output noise contribution from the resistors without significantly affecting the PZC net. The resistor $R_o = 50$ Ω was used for source-end impedance matching to the 50 Ω output transmission line. The critical input amplitude of OPA847 before the start of the slew rate limitation is $V_{crit}^{847} = 38.8$ mV. For 50 V/V gain, it corresponds to a 1.9 V output voltage. The full power bandwidth (FPB) of OPA847 at ±5 V power supply was $FPB_{847} = 45.8$ MHz.

In the Qint + NinvAmp configuration, the PZC circuit comprises $C_{pz}^{nin} = 1$ nF, $R_{pz}^{nin} = 1$ kΩ, and $R_{g2}^{nin} = 9.8$ Ω. Thus, condition $\tau_{rc}^{nin} = R_{pz}^{nin} C_{pz}^{nin} = \tau_{int}$ is satisfied. However, in the Qint + InvAmp configuration, the PZC circuit comprises $C_{pz} = 1$ nF, $R_{pz}^{inv} = 500$ Ω, and $R_{g1}^{inv} = 10$ Ω, which breaks the equality $\tau_{rc}^{inv} = R_{pz}^{inv} C_{pz}^{inv} \neq \tau_{int}$. If R_{pz}^{inv} was set to 1 kΩ to force equality, a significant overshoot would appear at the end of the decay edge. This might be due to the fact that the inverting input of the OPA847 is no longer at virtual ground

because of the presence of $R_{g2}^{inv} \| C_{g2}^{inv}$. By setting $R_{pz}^{inv} = 500\ \Omega$ in the present circuits, the overshoot and resultant overcompensation are both at the noise level. The decay time constant of the PZC output signal was $\tau_{pz} \approx 10$ ns.

For the input charge of 10^5 to 10^6 equivalent electrons, the Qint output pulse height is expected to be 3.2 mV to 32 mV. The PZC net roughly halves the amplitude to 1.6 mV and 16 mV due to the ballistic deficit. This signal is further amplified ±50 times in the following NinvAmp or InvAmp stages. Finally, the impedance-matching resistor R_o halves the voltage transmitted to the following 50 Ω transmission line. Therefore, the final output pulse height ranged from 40 mV to 400 mV. This corresponds to an estimated conversion gain of 2.5 mV/fC, which is consistent with the calibrated gain in Sect. 3.2.

2.2 Bandwidth and noise analysis

The circuit parameters are optimized to increase the SNR while preserving the detector's fast response information in the output signal, which requires balancing the signal front edge speed, noise level, and counting rate capability. The high GBWs and SRs of OPA657 and OPA847 guarantee a fast transient response such that the output signal front edge can follow the nanosecond detector response. The counting rate capability is limited by the signal decay time, which is determined by the frequency response (FR).

For the Qint + NinvAmp circuit, the FR is

$$H_{INV} = \frac{1}{2} H_{Qint} H_{pzc}^{nin} H_{NinvAmp}, \tag{1}$$

where H_{Qint}, H_{pzc}^{nin}, and $H_{NinvAmp}$ are the FRs of the Qint stage, PZC net, and NinvAmp stage, respectively. The coefficient 1/2 stems from impedance matching between the output terminal and the transmission line. Similarly, the FR of the Qint + InvAmp circuit is

$$H_{NINV} = \frac{1}{2} H_{Qint} H_{pzc}^{inv} H_{InvAmp}, \tag{2}$$

where H_{pzc}^{inv} and H_{InvAmp} are the FRs of the PZC net and the InvAmp stage, respectively. The relevant amplitude-frequency responses (AFRs) are shown in Fig. 4.

The passbands of the Qint + NinvAmp and Qint + InvAmp circuits can be identified from the AFR curves as 160 kHz to 16 MHz and 300 kHz to 16 MHz, respectively. The lower frequency region was suppressed by the Qint band-pass filter, the passband of which was 90–560 kHz. The high-frequency –3 dB bandwidths of the overall circuits are much larger than those of the Qint circuit because the PZC net is a high-pass filter with a bandwidth of 16 MHz. Furthermore, the bandwidths of the NinvAmp and

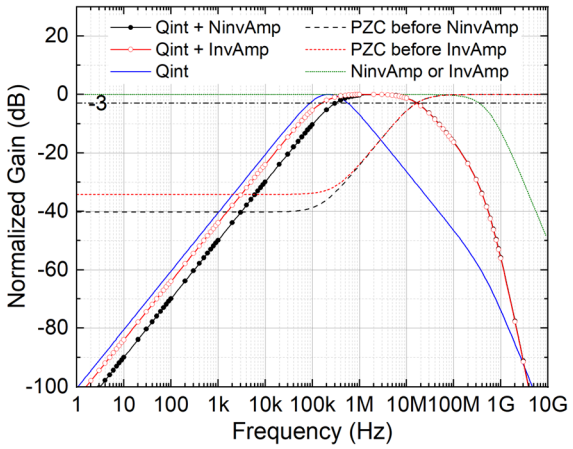

Fig. 4 AFRs of the CSAs and subcircuits. All curves were normalized to 0 dB. The -3dB gain is indicated with a dash-dot line

InvAmp circuits are 340 MHz. They do not contribute to the overall bandwidth and ensure that the signals from the PZCs can be amplified linearly. The 16 MHz high-frequency –3 dB bandwidth of both CSAs results in a signal decay edge of ~ 22 ns, which ensures that the CSAs can operate at high counting rates.

However, controlling the noise level of the Qint stage is key to improving the SNR of the final output, which also benefits from the PZC high-pass filter. Taking Qint + NinvAmp CSA, for instance, the noise model of Qint with PZC is shown in Fig. 5. The symbols i_{657}^2 and v_{657}^2 denote the power spectra densities (PSDs) of the equivalent current noise and voltage noise of the OPA657 amplifier, respectively, i_d^2 is the PSD of the detector leakage current noise, $i_{Rd}^2 = \frac{4kT}{R_d}$, $i_{Rc}^2 \approx \frac{4kTR_c}{R_d^2} \cdot (1 + 4\pi^2 f^2 R_d^2 C_d^2)$, $i_{Rg1}^2 \approx \frac{4kT}{R_{g1}^{int}} \cdot (2\pi f R_{g1}^{int} C_{g1}^{int})^2$, and $i_{Rf1}^2 = \frac{4kT}{R_{f1}^{int}}$ represent the PSDs of the thermal current noises of corresponding resistors, and v_o^2 is the PSD of the output voltage noise. Here, k is the Boltzmann constant, T is the absolute temperature, i_{Rc}^2 is derived by considering that in the passband of the linear amplification stage, the impedance of $R_d \| C_d$ is much larger than that of R_c and C_c in series, and i_{Rg1}^2 is calculated by assuming that the impedance of C_{g1}^{int} is much larger than R_{g1}^{int} in the passband. Furthermore, because the impedance of C_d is much larger than those of C_c and R_c in series in the passband, i_d^2 and i_{Rd}^2 can be equivalently moved to the OPA657 inverting input pin (in parallel with i_{657}^2). Thus, the total input current noise is $i_i^2 = i_d^2 + i_{657}^2 + i_{Rd}^2 + i_{Rc}^2 + i_{Rg1}^2$, and the input voltage noise is $v_i^2 \equiv v_{657}^2$. The output noise of the PZC net is $v_o^2 = (|A_n|^2 v_i^2 + |A_s|^2 i_i^2)|H_{pzc}^{nin}|^2$, where A_n and A_s are the noise and signal gains of the integration circuit, respectively.

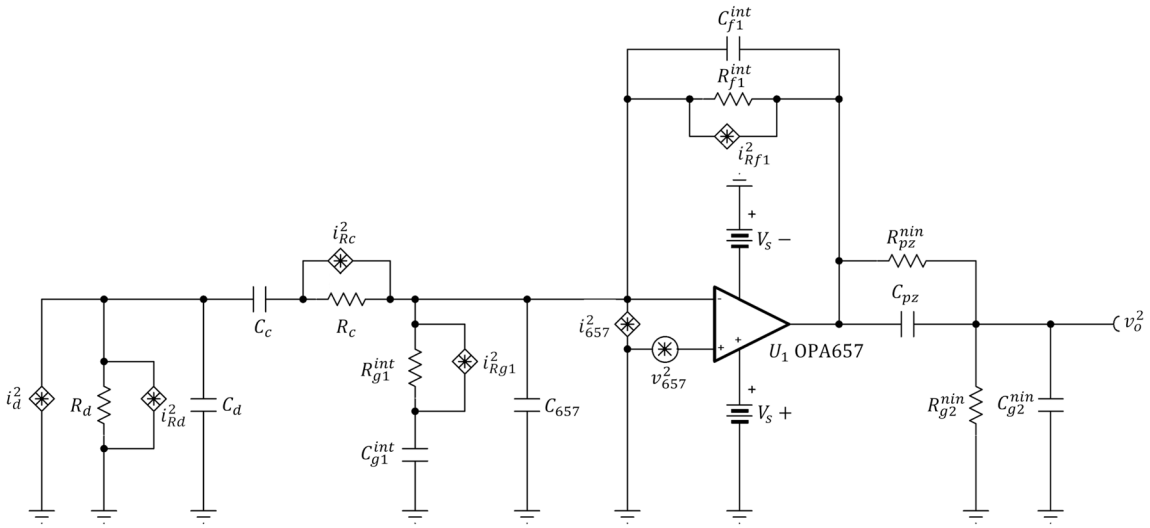

Fig. 5 Noise model of the Qint stage with PZC net. The star-inside-diamond symbols represent the current noise sources. The star-inside-circle symbol represents the voltage noise source

By disregarding the detector leakage current noise and substituting $i_{657} = 1.3\ \mathrm{fA}/\sqrt{\mathrm{Hz}}$, $v_{657} = 4.8\ \mathrm{nV}/\sqrt{\mathrm{Hz}}$, $T = 300$ K (room temperature), and other relevant variables as shown in Fig. 6 shows the input voltage noise, input current noise, and overall input noise contributions to v_o^2 for different $R_{\mathrm{fl}}^{\mathrm{int}} \| C_{\mathrm{fl}}^{\mathrm{int}}$ combinations. In $R_{\mathrm{fl}}^{\mathrm{int}} = 2\ \mathrm{k\Omega}$, $C_{\mathrm{fl}}^{\mathrm{int}} = 5$ pF, no PZC net was inserted. For the other cases, the PZC net was the same as that shown in Fig. 3a, except for resistor $R_{\mathrm{pz}}^{\mathrm{nin}}$, which is adjusted to match $R_{\mathrm{fl}}^{\mathrm{int}} C_{\mathrm{fl}}^{\mathrm{int}}$. As shown, $R_{\mathrm{fl}}^{\mathrm{int}} = 200\ \mathrm{k\Omega}$ and $C_{\mathrm{fl}}^{\mathrm{int}} = 5$ pF yielded the best results. The total low-frequency and high-frequency PSDs were dominated by the input current and voltage noise contributions, respectively. By decreasing $R_{\mathrm{fl}}^{\mathrm{int}}$ to 20 kΩ, the total low-frequency noise increases owing to a higher input voltage noise contribution. By decreasing $C_{\mathrm{fl}}^{\mathrm{int}}$ to 1 pF, the total noise PSD significantly increased across the entire frequency range. In the low-frequency region, the input current noise contribution increased significantly, whereas in the high-frequency region, both the input voltage and current noise contributions increased significantly. In the $R_{\mathrm{fl}}^{\mathrm{int}} = 2\ \mathrm{k\Omega}$ and $C_{\mathrm{fl}}^{\mathrm{int}} = 5$ pF cases, the PZC net was removed, but the decay time constant of the Qint output was still 10 ns (the same as that of the PZC output in the other cases). It represents the worst case in the low-frequency range because of the

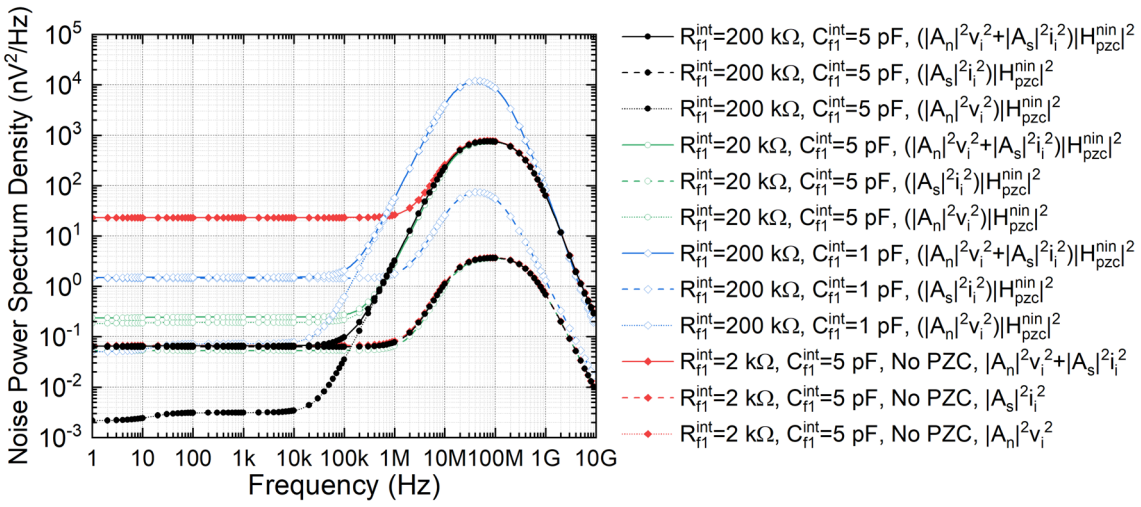

Fig. 6 Voltage noise PSDs at the input of the OPA847 stage. In $R_{\mathrm{fl}}^{\mathrm{int}} = 2\ \mathrm{k\Omega}$, $C_{\mathrm{fl}}^{\mathrm{int}} = 5$ pF, no PZC net was inserted. For the other $R_{\mathrm{fl}}^{\mathrm{int}} \| C_{\mathrm{fl}}^{\mathrm{int}}$ combinations, the PZC net is the same as in Fig. 3a except for the resistor $R_{\mathrm{pz}}^{\mathrm{nin}}$, which is adjusted to match $R_{\mathrm{fl}}^{\mathrm{int}} C_{\mathrm{fl}}^{\mathrm{int}}$

increase in the input voltage noise contribution. The input current noise contribution is almost the same as that in $R_{\mathrm{fl}}^{\mathrm{int}} = 200\,\mathrm{k}\Omega$ and $C_{\mathrm{fl}}^{\mathrm{int}} = 5\,\mathrm{pF}$ over the entire frequency range. The above analyses led to the present design: a relatively large $C_{\mathrm{fl}}^{\mathrm{int}}$ and $R_{\mathrm{fl}}^{\mathrm{int}}$ in conjunction with a PZC high-pass filter.

2.3 PCB layout and routing

On a rectangular 10 cm×20 cm PCB, 4 × 8 preamplifiers are realized in a planar array, as shown in Fig. 7. The pad layout and routing were the same for each unit. By setting some pads DNP (do not populate), there is considerable flexibility in adjusting circuits. Thus, both the CSA circuits can be implemented. In Fig. 7, the 1st and 3rd rows are the Qint + NinvAmp amplifiers, while the 2nd and 4th rows are the Qint + InvAmp circuits. At the input and output, the signals were routed through a surface-mounting board-to-board (BTB) connector. The adjacent signal pins on each connector are isolated by a pair of pins that are independently connected to the power and ground planes. This pin configuration minimizes the connector-mediated crosstalk, unifies the signal return path, and contributes to reducing the power-ground impedance. The two LEMO connectors soldered on the bottom were used for the power supply in the circuit test phase.

The stack consists of ten layers, as listed in Table 2. The second and bottom layers were ground planes for better electromagnetic compatibility (EMC). Between them, four signal layers are interleaved with the ground or power planes. Thus, all 32 input and 32 output signal traces were striplines routed in parallel. The impedance of the signal traces was adjusted to 50 Ω with the trace width set to 9 mil. The minimum separation between two adjacent traces parallel to the PCB surface is at least 120 mil when they are on the same layer, 60 mil when they are on adjacent signal planes, and 0 when they are three layers apart. Except for 16 parallel signal traces (eight input and eight output) on each signal plane, the remaining area was filled with grounded copper, which provided even better decoupling for the power planes. In addition, stitching vias were placed around each amplifier cell along the PCB border and on both sides of every signal trace.

Table 2 PCB stackup design. GND denotes the ground plane. PWR denotes the power plane

Layer	Routing
1 (top)	component layer
2	GND
3	signal
4	PWR, +5 V
5	signal
6	GND
7	signal
8	PWR, –5 V
9	signal
10 (bottom)	GND with a few components

2.4 Power consumption and heat dissipation

In all subsequent laboratory tests, the ±5 V power supplies of the OPAs were provided by the Rohde & Schwarz HMP4040 regulated power supply, which has an RMS voltage ripple of less than 1.5 mV [44]. Moreover, three parallel decoupling capacitors, 10 µF‖100 nF‖1 nF are installed close to each power pin of each OPA. The maximum quiescent power consumptions of OPA657 and OPA847 were 163 mW and 189 mW, respectively, at ±5 V power supply [42, 43]. In comparison, the power consumption of the other passive components was negligible. Therefore, the quiescent power of each channel should be less than 352 mW. This is in agreement with the measurement at 319 mW. In addition, the power consumption under the following operating conditions was measured.

The 32-channel CSA under test was placed in a 34 cm × 23.5 cm × 16 cm metal shielding box, which also entirely prevented the airflow. It is connected to the box via coaxial

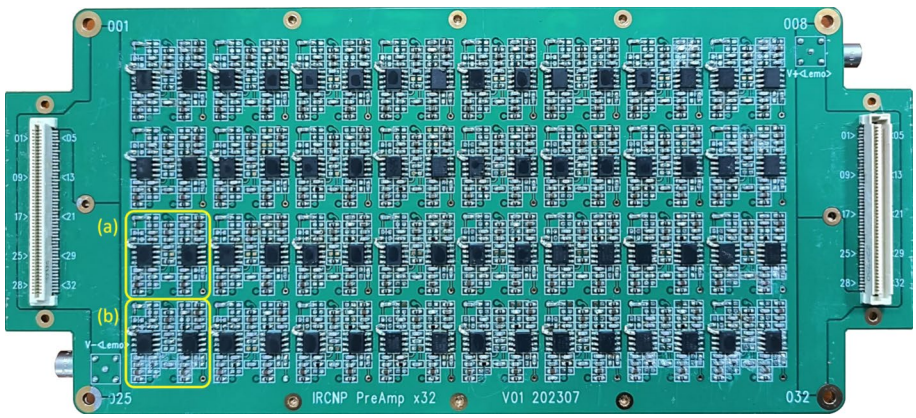

Fig. 7 (Color online) Photograph of the PCB. The 1st and 3rd rows are Qint + NinvAmp amplifiers. The 2nd and 4th rows are Qint + InvAmp circuits. **a** and **b** indicate the Qint + NinvAmp and Qint + InvAmp channels used in the following performance tests, respectively

signal cables at the input, output, and power supply connectors; via screws at the four corners; and via copper cables at the six via holes along the PCB edges. All channels were simultaneously driven in the same manner using a 1 MHz excitation signal. The amplitudes of the 32 output signals were 1 V. The load resistor of each channel is 50 Ω. After stabilization, the power consumption per channel was 321 mW, which is slightly higher than the quiescent power.

After one hour of continuous operation, the temperature distribution on the CSA surface was measured using a Fluke iSee TC01A thermal-imaging camera [45]. As shown in Fig. 8, the highest temperature, 62.1°, occurred in the OPA package. The measurements were performed at 25° ambient temperature and a camera-to-CSA distance of 25 cm. The infrared emissivity was set to 0.9 according to the materials of the chip package and PCB solder mask. Every channel works stably during several hours of continuous operation. Hence, the CSA is qualified for long-term operation in air at room temperature under the condition that proper connections with the shielding box are made as above.

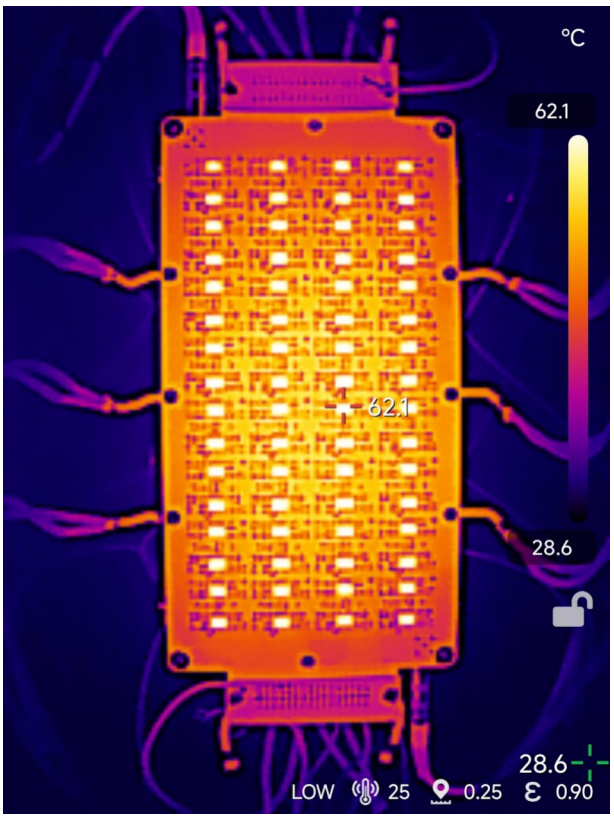

Fig. 8 (Color online) Temperature distribution on the CSA surface after one hour of continuous operation. The CSA was placed in a metal shielding box and connected via screws or cables. All channels were simultaneously driven in the same manner as a 1-MHz excitation signal. The amplitudes of the 32 output signals were approximately 1 V. The ambient temperature is 25°

3 Performance tests

The Qint + NinvAmp and Qint + InvAmp channels used in the performance calibrations are shown in Fig. 7a and b. Typical waveform outputs of the CSAs are presented in Fig. 9 together with the input charge signals. These are calculated as follows: a resistor $R_{test} = 2$ kΩ is connected in series with capacitor C_c, and a pull-down resistor to the GND, $R_{gnd} = 10$ Ω, is installed between them, as shown in the inset of Fig. 9. By calculation, the introduction of R_{test} and R_{gnd} only slightly modified the FR system. A fast negative voltage pulse was fed to each CSA through R_{test}. This resistor converts the voltage pulse into a current pulse, and the input charge signal is simply an integration of the current pulse. The rising time, falling time, and full width at half maximum of the input voltage pulse were 2 ns, 2 ns, and 3 ns, respectively. The leading edges of the input charge signal, the Qint + NinvAmp output, and the Qint + InvAmp output signals are 3.3 ns, 3.8 ns, and 4.1 ns, respectively. Meanwhile, their amplitudes are –576 fC, 1.02 V, and −1.18 V, respectively. As expected from the analyses in Sect. 2.2, the leading edges of the output signals can follow nanosecond input charge variation, and the decay edges are in agreement with the prediction of the system AFR.

The input voltage pulse is generated using a Tektronix AFG 31252 signal generator [46]. The output waveforms were acquired with a Rohde & Schwarz MXO44 oscilloscope [47] (HD mode: 14-bit analog-to-digital converter (ADC), 300 MHz bandwidth, 2.5 GS/s sampling rate). In the following performance tests, the signal generator and oscilloscope used were the same as above, except for the noise, baseline, and time-resolution measurements.

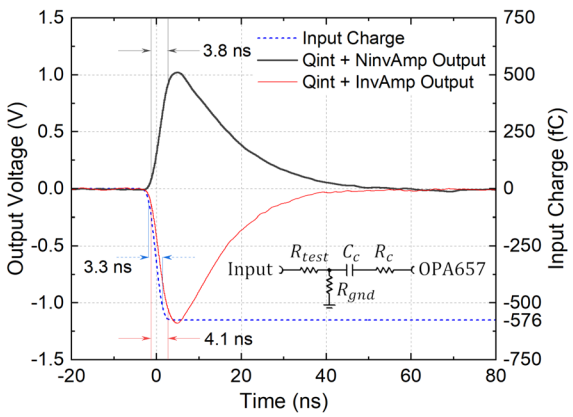

Fig. 9 A sample of an input charge signal (dash) and the corresponding output voltage signals by the Qint + NinvAmp (positive pulse in thick solid line) and Qint + InvAmp (negative pulse in thin solid line) amplifiers. The input charge signal is simulated by applying a fast negative voltage pulse to the "Input" of the inset circuit diagram

3.1 Bandwidth

Sinusoidal voltage signals with frequencies ranging from 10 kHz to 100 MHz were fed into each circuit via the R_{test} resistor. The average amplitude of the output signals was measured using an oscilloscope. The AFRs are shown in Fig. 10. From the curves, the passbands of the Qint + NinvAmp and Qint + InvAmp circuits were determined to be 270 kHz–13 MHz and 104 kHz–15 MHz, respectively, which are consistent with the theoretical AFRs.

3.2 Linearity

The input charge signals are generated in the same manner as in Fig. 9, differing only in the total input charge. The evolution of the average output pulse amplitude with respect to the total input charge is shown in Fig. 11. The conversion gain is determined by fitting the corresponding data, which are −1.78 mV/fC and 2.02 mV/fC for the Qint + NinvAmp and Qint + InvAmp circuits, respectively. The measured input ranges are −96 fC to −864 fC and −48 fC to −720 fC. The corresponding linear correlation coefficients are −0.99995 and 0.99981, respectively. The corresponding integral nonlinearities were ±0.5% and ±0.7%. The energy deposition of an incident particle inside a PPAC and the charge avalanche amplification exhibit considerable fluctuations that are much larger than the measured integral nonlinearities. Hence, the proposed circuit linearities are acceptable.

3.3 Noise and baseline

The detector capacitance C_d is simulated with a capacitor soldered between the channel input pad and ground pad under the input BTB connector. The RMS noise and offset

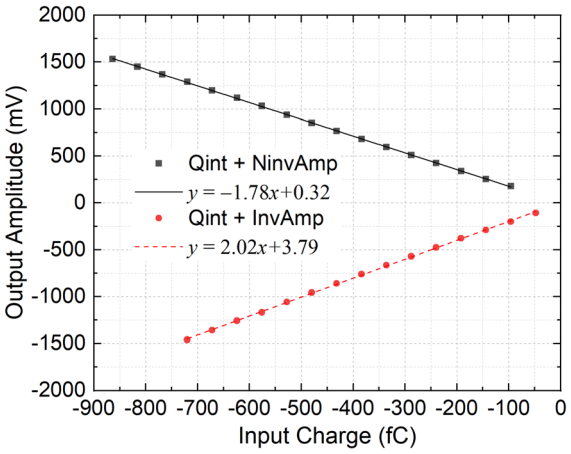

Fig. 11 Variation of the output pulse amplitude with the total input charge for the Qint + NinvAmp and Qint + InvAmp circuits, respectively

of the signal baseline were measured using the statistical function of the Keysight InfiniiVision MSOX6004A oscilloscope [48] (HD mode: 12-bit ADC, 1 GHz bandwidth, 20 GS/s sampling rate), which are the standard deviation and mean of the baseline statistics, respectively. During the measurements, the time range of the oscilloscope was set as −1 µs ∼ 1 µs. The voltage ripple of the HMP4040 power supply had no observable influence on the noise and baseline performance, as verified by substituting it with lithium-ion batteries. The results are shown in Fig. 12. Each dataset is fitted using a cubic polynomial. For the Qint + NinvAmp and Qint + InvAmp circuits, the zero-capacitance RMS noises are 5.85 mV and 6.59 mV, respectively. They correspond to the equivalent noise charges (ENCs) of 3.29 fC and 3.26 fC, respectively. The noise evolution is dominated by the

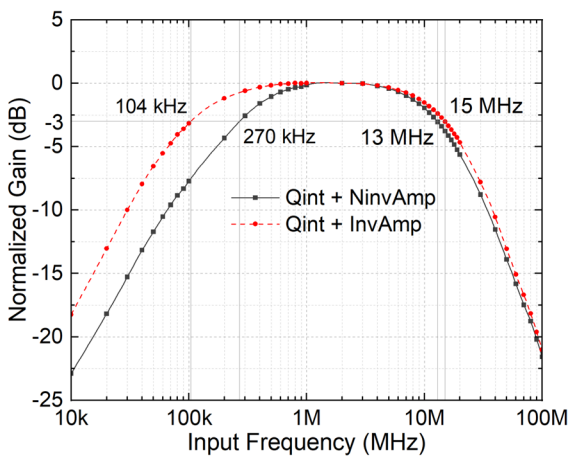

Fig. 10 Measure AFRs of the Qint + NinvAmp and Qint + InvAmp circuits. Frequencies annotated by the side of the vertical reference lines indicate corresponding -3dB bandwidths

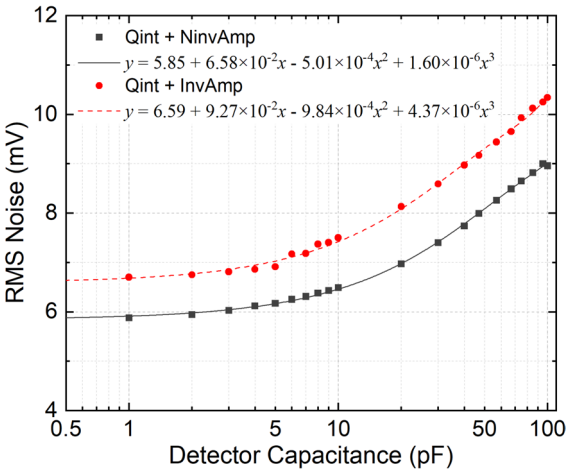

Fig. 12 Evolution of the CSA output RMS noise with the detector capacitance. The detector capacitance is mimicked by a capacitor soldered on the back side of the input BTB connector

linear coefficients, which are 6.58×10^{-2} and 9.27×10^{-2}. The noise evolution is further modified by the quadratic coefficients -5.01×10^{-4} and -9.84×10^{-4} and the cubic coefficients 1.60×10^{-6} and 4.37×10^{-6}, respectively. The maximum baseline shift of each output with varying detector capacitance is 1.35 mV and 6.12 mV, respectively, both of which are smaller than the corresponding RMS noise.

3.4 Crosstalk

The crosstalk between any two channels is measured as follows: The charge signal is identical to that shown in Fig. 9 was fed to one channel through R_{test}. A 50 Ω load resistor was pre-installed at the output of the channel immediately under the output BTB connector. The outputs of any other channel are then observed using an oscilloscope via the corresponding pins of the output BTB connector. The waveforms did not show any differences in the presence of the input charge signal. Hence, it can be concluded that crosstalk, if any, is completely masked by the noise.

3.5 Timing accuracy

The bandwidth, linearity, noise, and baseline shift of the CSAs contribute to the timing accuracy of the detection system, which is the ultimate requirement of the PPAC array under development. The timing accuracy is also influenced by the detector response and the back-end data acquisition system. To calibrate the CSA contribution to the timing accuracy, a capacitor $C_{\text{test}} = 5$ pF (instead of the resistor R_{test}) was installed in series with the capacitor C_{c}, and the resistor R_{gnd} was removed. An exponentially decaying voltage pulse was supplied to C_{test}. The transient rising edge of this excitation signal stimulates a current pulse in C_{test}, which simulates the detector response. This signal injection scheme was used instead of the one shown in the inset of Fig. 9 because the thermal noise of the resistor R_{gnd} introduces a large current noise at the OPA657 input pin, which evidently deteriorates the CSA timing accuracy. In contrast, the insertion C_{test} has little influence on the noise level. Moreover, although C_{test} moves the passband of the CSAs to 15 MHz ~ 242 MHz according to the AFR, the final output signal rising edge is 4.5 ns in the present test, which is close to our measurement in Fig. 9, where the system passband was not modified.

In the measurement, a pair of Qint + NinvAmp channels or Qint + InvAmp channels was tested. Two 128 kHz exponentially decaying excitation signals are fed to the channels, with a relative delay of several nanoseconds. The amplitudes of the excitation signals were tuned such that the amplitudes of the two CSA output signals were both −1 V. The two output signals were acquired using an oscilloscope (Tektronix DPO5034B [49]; 350 MHz bandwidth, 5 Gs/s sampling rate) with a sampling interval of 10 ps. Subsequently, the two waveforms were analyzed offline using a constant fraction discrimination algorithm, from which the time difference was calculated. In total, 2000 pairs of waveforms were analyzed for both the Qint + NinvAmp and Qint + InvAmp cases. The distributions of the time differences are shown in Fig. 13 with the mean time difference shifted to zero. The same test and analysis methods were applied to a commercial preamplifier module, FTA820A [50], in which the excitation signal amplitudes were also tuned to ensure that the output signal amplitudes were −1 V.

Histograms were fitted using Gaussian functions. The standard deviations of the fitting results for the Qint + NinvAmp, Qint + InvAmp, and FTA820A amplifiers are 50.4 ps, 45.3 ps, and 13.7 ps, respectively. The time resolutions of a single channel were obtained by dividing them by $\sqrt{2}$, which were 35.6 ps, 32.0 ps, and 9.7 ps, respectively. The FTA820A module is a well-known current-sensitive amplifier with a gain of ~ 20 mV/μA, a bandwidth of 10 MHz to 350 MHz, and ≤ 20 μV RMS equivalent input noise [50], which is the best preamplifier available in our laboratory. In comparison, the intrinsic time resolutions of the Qint + NinvAmp and Qint + InvAmp CSAs are relatively inferior, yet still much better than the 350 ps requirement for the overall timing accuracy. Moreover, as described in Sect. 4, the position resolutions of the PPAC prototype are essentially the same, regardless of whether the FTA820 or the present CSAs are used.

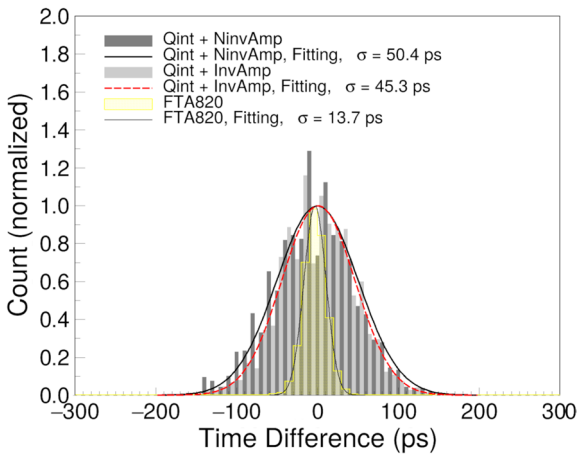

Fig. 13 The time difference distributions between two channels of the Qint + NinvAmp (dark gray), Qint + InvAmp (light gray), and FTA820A (yellow hatching) amplifiers. The thick solid, dash, and thin solid curves are fitted to the histograms

4 Application in PPAC

The practicality of the CSAs was verified using a custom-made PPAC. It is a prototype of one unit of the PPAC array under development and is used as a proof of principle. It primarily consists of a cathode membrane and an anode readout PCB, as shown in Fig. 14. They were parallel at a distance of 9 mm. The membrane was a double-sided, aluminum-coated Mylar film. The thickness of the Mylar material is 2 μm. The thickness of the two aluminum layers was 300 nm. The top layer of the readout PCB was a 61×61 array of square copper pixels. Adjacent pixels belong to two orthogonal dimensions, namely, the x or y dimension, with no electrical connection between them other than parasitic ones. Along each dimension, the pixels were connected by copper traces on the inner PCB layers, forming pixel strips that were further connected with a delay line. Hence, the Cartesian coordinates (x, y) of an incident particle can be read independently using two delay lines. Each delay line consisted of a series of inductors and capacitors that simulated an actual transmission line. The sensitive area of the detector was 61 mm × 61 mm, pixel repetition period was 1 mm, and delay time between adjacent pixel strips was 4 ns. The total delay time of each delay line was 240 ns.

During the test, the membrane was supplied with −1 kV high voltage, and each delay line was grounded with 1 MΩ resistors at both ends. The detector was filled with 7.6 mbar iC_4H_{10} gas, and the entire detector was placed in a vacuum chamber of 3×10^{-2} mbar. An aperture mask of 2 mm thickness was installed on top of the membrane, the pattern of which is also shown in Fig. 14. Alpha particles of 5.4 MeV energy passing through the apertures were detected. The alpha particles were obtained from a ∅5 cm circular array of 50 ^{241}Am radiation sources, which were placed 10 cm in front of the aperture mask. The average counting rate was 286 s^{-1}.

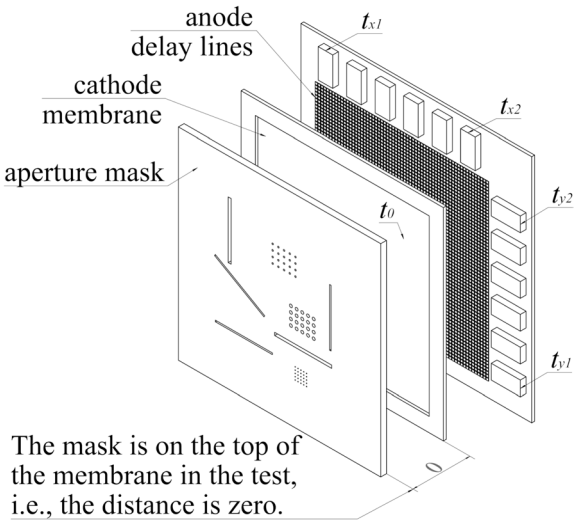

Fig. 14 Sketch of the PPAC used in the test. The index arrows beside t_0, t_{x1}, t_{x2}, t_{y1}, and t_{y2} indicate the positions from which the corresponding time signals are read out

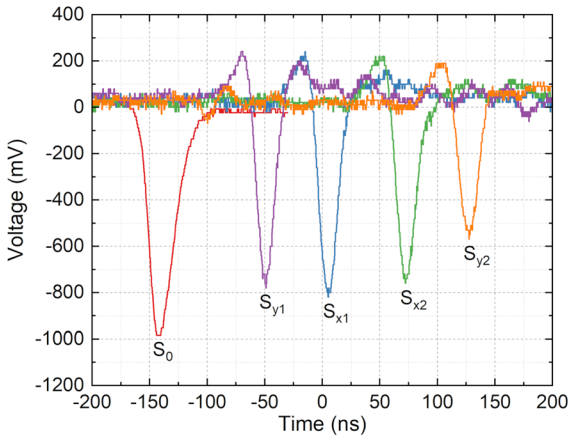

Fig. 15 (Color online) Waveforms from one Qint + NinvAmp amplifier (S_0) and four Qint + InvAmp amplifiers ($S_{x1}, S_{x2}, S_{y1}, S_{y2}$). S_0 is the signal from the membrane during an event. S_{x1} and S_{x2} (S_{y1} and S_{y2}) are the signals from the delay-line in the $x(y)$ direction in another event

Typical waveforms from CSAs are shown in Fig. 15. The trigger signal (S_0) was read out from the membrane using a Qint + NinvAmp amplifier. The other four signals ($S_{x1}, S_{x2}, S_{y1}, S_{y2}$) are read from the two delay lines using four Qint + InvAmp amplifiers. Note that the membrane signal and remaining delay-line signals are from two events with no temporal correlation. They are shown together to illustrate the common temporal sequence, that is, the membrane signal precedes the delay-line signals. The leading small positive peak and the following large negative peak in each delay-line signal indicate that the output current pulses from the delay lines are bipolar, which may be caused by the induction between the membrane and the anode.

The five analog signals from the CSAs were fed to a constant fraction discriminator, the ORTEC CF8000 [51]. The five logic signals from the discriminator were further processed using the CAEN time-to-digital converter (TDC) module V775 [52]. The digital times of the four delay-line signals, t_{x1}, t_{x2}, t_{y1}, and t_{y2} are measured relative to the trigger time t_0, the latter of which signifies the particle arrival time. For comparison purposes, the same test procedure was performed using the FTA820A module.

The distributions of $t_{x1} + t_{x2}$ and $t_{y1} + t_{y2}$ represent the time resolutions of the delay lines in the X- and Y-directions, respectively. They are shown in Fig. 16, where the mean is shifted to zero. The gray histograms and histograms with no fill were obtained with the designed CSA and FTA820A module, respectively. Dividing the standard

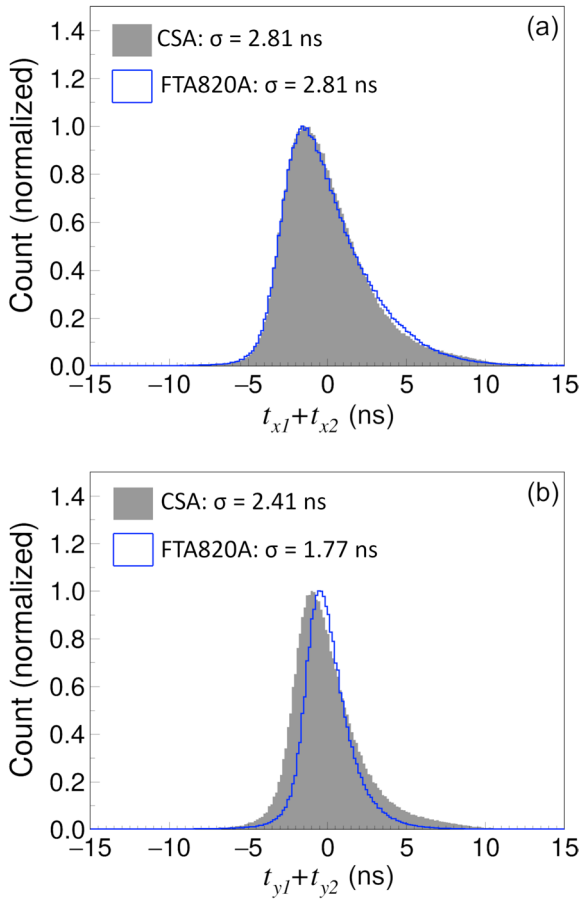

Fig. 16 Distributions of **a** $t_{x1} + t_{x2}$ and **b** $t_{y1} + t_{y2}$, respectively. Gray histograms were obtained using the designed CSA. The histograms with no fill are obtained with the FTA820A preamplifier

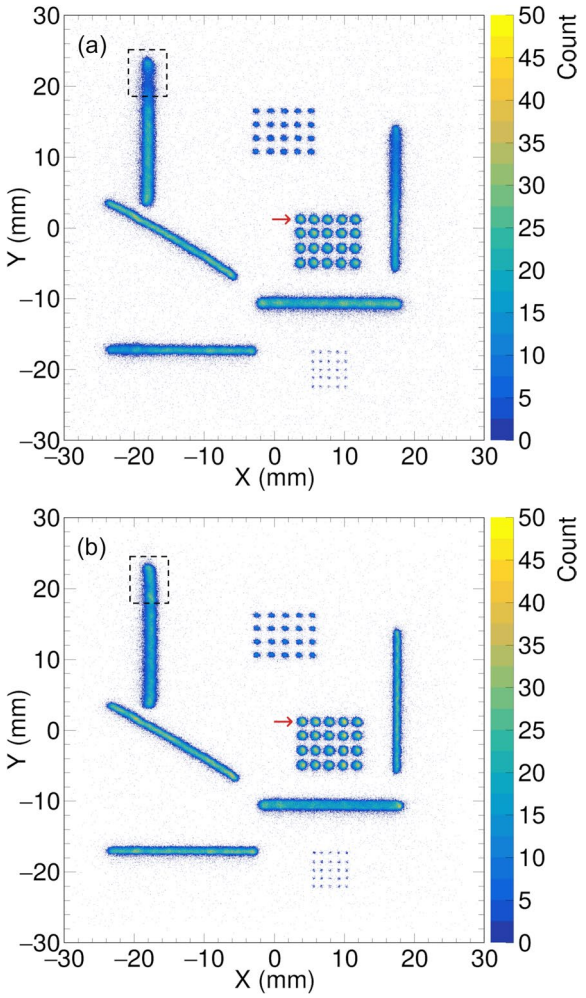

Fig. 17 (Color online) Position spectrums measured in the test with **a** the designed CSA and **b** the FTA820A module. The arrow in each subplot indicates the aperture data used for the position resolution analysis. The dashed rectangle in each subplot indicates the position distribution distortion

deviations by $\sqrt{2}$ yields the corresponding time resolutions of the single-delay-line channels. The CSA is $\sigma^x_{\mathrm{CSA}} = 1.99$ ns and $\sigma^y_{\mathrm{CSA}} = 1.70$ ns in the *X*- and *Y*-directions, respectively. For FTA820A, these are $\sigma^x_{\mathrm{FTA}} = 1.99$ ns and $\sigma^y_{\mathrm{FTA}} = 1.25$ ns, respectively. The CSA performance in both directions was more uniform than that of the FTA820A module, whereas in the Y direction, FTA820A exhibited better performance. This might be explained by the fact that the transfer functions of CSA and FTA820A are very different, causing the coupling of the delay line with them to fold the event time information into the amplifier output signals in distinct ways. In addition, the delay-line time resolutions were much larger than the intrinsic timing accuracies of CSA and FTA820A, indicating that they were dominated by the detector itself.

The position coordinates are calculated as $x = \frac{t_{x1}-t_{x2}}{t_{x1}+t_{x2}-t_{xs}} \times HL$ and $y = \frac{t_{y1}-t_{y2}}{t_{y1}+t_{y2}-t_{ys}} \times HL$. $HL = 30$ mm is the half-width of the detector in the x and y directions. t_{xs} and t_{ys} are calculated by fitting the measured pattern to the real mask geometry, which are $t_{xs} = 3271$ and $t_{ys} = 3234$ for CSA, and $t_{xs} = 3156$ and $t_{ys} = 3117$ for FTA820A. Figure 17a and b show the 2D position spectra obtained using CSA and FTA820A, respectively. Both faithfully matched the aperture masks. The dashed rectangle in each subplot indicates a position distribution distortion. In (a), the distortion presents as a detection efficiency degradation, whereas in (b), it appears as a position shift to the detector edge. This is a finger effect, that is, the inductors and capacitors near the delay-line ends are too few to emulate a real transmission line.

The position resolutions were further analyzed as follows: Taking Fig. 17a for instance, the arrow indicates the position distribution $h(x, y)$ used for position resolution analysis, which is enlarged in Fig. 18a. It is formed by particles passing through the corresponding aperture.

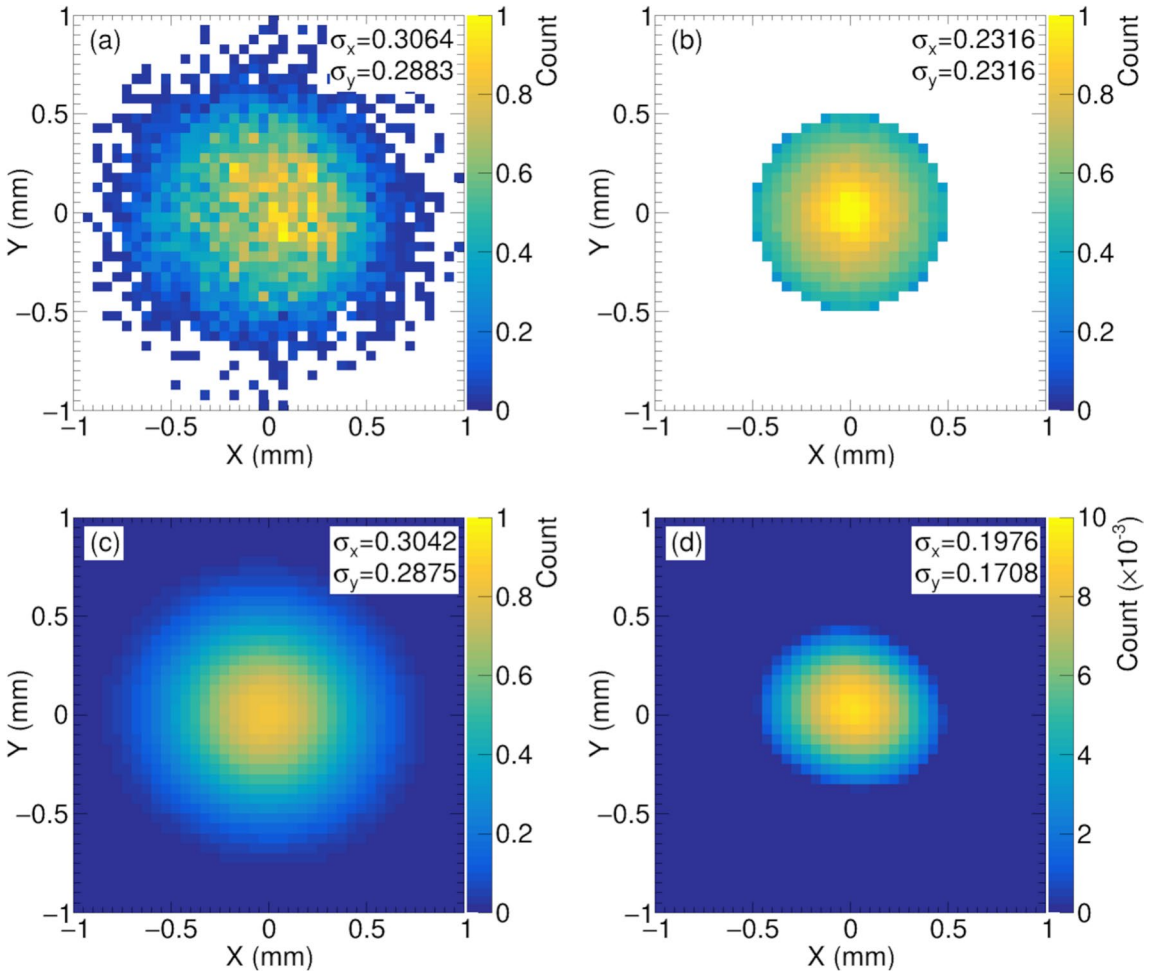

Fig. 18 (Color online) Position resolution analysis with the CSA data. **a** Enlarged plot of the distribution indicated by the arrow in Fig. 17a. **b** Geant4 simulation of position distribution where particles pass through the detector membrane covered by the aperture. **c** Convolution of **b** and **d**. **d** Detector resolution function deconvolved from **a** using kernel **b**. For each distribution, σ_x and σ_y are the standard deviations in the X and Y directions, respectively

On the other hand, the distribution $g(x, y)$ of the positions where these particles pass through the detector membrane is simulated with the Geant4 software [53], which is shown in Fig. 18b. The position resolution function $\rho(x, y)$ is then obtained by deconvolving $h(x, y)$ with the kernel $g(x, y)$, as shown in Fig. 18d. The distributions shown in Fig. 18c is $g(x, y) * \rho(x, y)$, which fits $h(x, y)$. The standard deviations of the four distributions are shown in the figures. For the $\rho(x, y)$ distribution, the detector position resolutions were defined as $\sigma_x^{\mathrm{CSA}} = 0.20$ mm and $\sigma_y^{\mathrm{CSA}} = 0.17$ mm in the X and Y directions, respectively. The same calculation was performed for the FTA820A data, as shown in Fig. 19. The position resolutions were $\sigma_x^{\mathrm{FTA}} = 0.20$ mm and $\sigma_y^{FTA} = 0.17$ mm in the X and Y directions, respectively. From the analyses of $t_{x1} + t_{x2}$, $t_{y1} + t_{y2}$, and the position resolutions, it can be concluded that CSA and FTA820A are equally applicable to the present PPAC.

Finally, the CSA exhibited excellent stability during the position spectra data acquisition process, which lasted for several hours at RT.

5 Summary

In summary, a 32-channel CSA was designed for a PPAC array under development for Coulomb excitation studies on atomic nuclei. This is realized on a 10 cm × 20 cm PCB with OPAs and other discrete components. Each channel mainly consists of an integrator, PZC net, and linear amplification stage, which can be configured to accommodate either positive or negative inputs. The performance parameters of CSA are listed in Table 3. In the prototype PPAC application, the CSA performs as well as the commercial FTA820A amplifier, providing a position resolution as good as 0.17 mm and

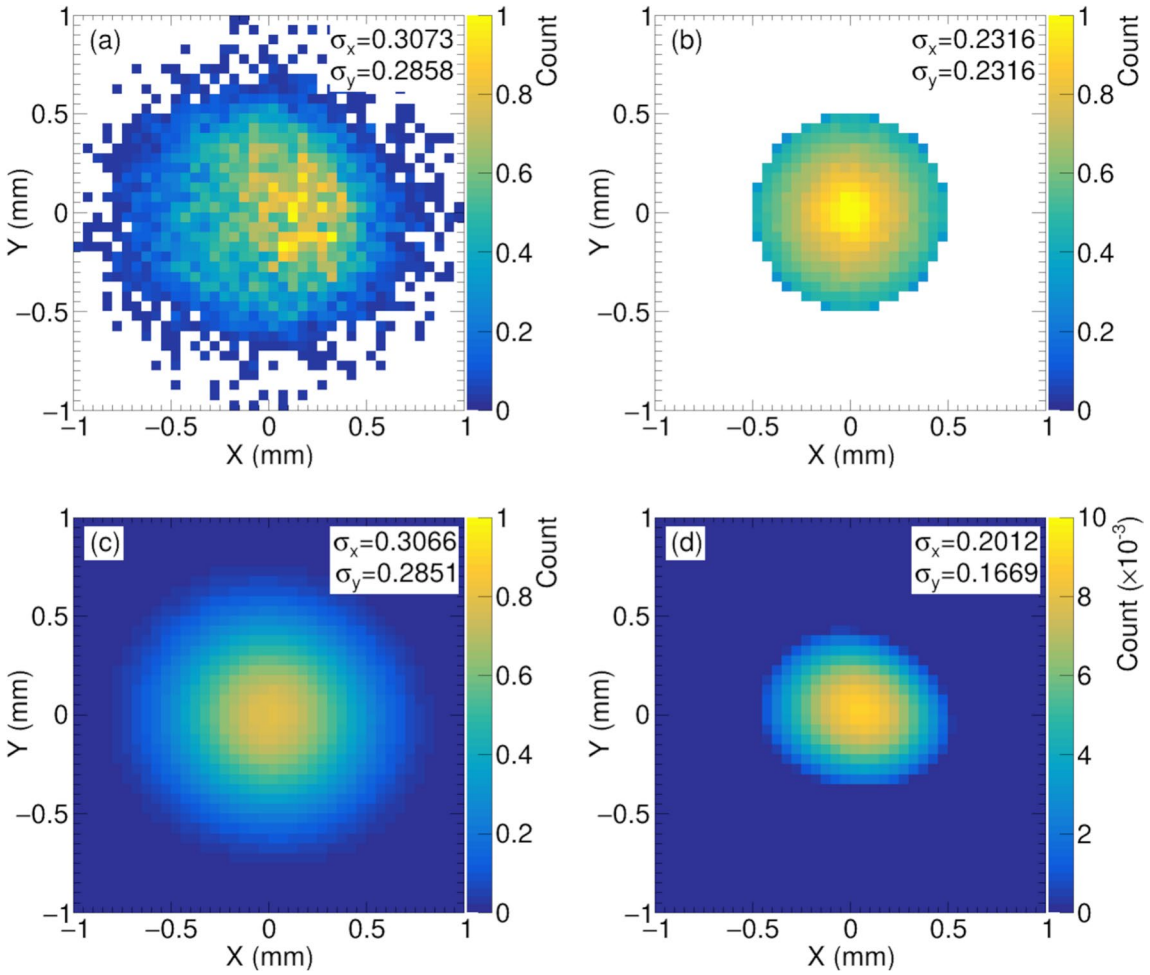

Fig. 19 (Color online) Position resolution analysis with the FTA820A data. Same as Fig. 18, but the position distribution under analysis is that indicated by the arrow in Fig. 17b

Table 3 CSA Performance Parameters

Parameter	Qint + NinvAmp	Qint + InvAmp
Dynamic range (fC)	−864	−720
Conversion gain (mV/fC)	−1.78	2.02
Integral nonlinearity	±0.5%	±0.7%
Leading edge	as low as 3.8 ns	as low as 4.1 ns
Bandwidth (Hz)	270k~13 M	104k~15 M
RMS noise (mV)	5.85	6.59
ENC (fC)	3.29	3.26
Baseline shift (mV)	<1.35	<6.12
Crosstalk	not observed	not observed
Timing accuracy (ps)	35.6	32.0
Power (mW)	321	321

exhibiting reliable stability during several hours of continuous data acquisition. Both the CSA intrinsic time resolution and detector position resolution were one order of magnitude better than the requirements. Compared to the FTA820A module, CSA offers the critical advantage of high integrity, which is essential for the 100-channel PPAC array.

Acknowledgements The authors are grateful for the support of the nuclear detector group at the Institute of Modern Physics, Chinese Academy of Sciences. Special appreciation goes to Prof. De-Yang Yu and Dr. Wei Zhou for their valuable suggestions on the amplifier design and the manuscript.

Author Contributions The physical background, essentiality, funding support, and administration of this work were laid mainly by the corresponding author Shou-Yu Wang. The determination of the amplifier parameters, schematic design, PCB design, and performance calibrations were carried out by Yue-Zhao Zhang. The amplifier timing accuracy was measured by Peng Ma. The amplifier-PPAC joint test was accomplished by Yuezhao Zhang and Peng Ma together, with the support of Zhuang-Yu Lin. Zhen-Fei Tan contributed to part of the amplifier calibration work. The work of En-Hong Wang greatly improved the language expression of the manuscript. All the other authors contributed to this work in background investigation, data validation, manuscript preparation, or resources to some extent.

Data Availability The data that support the findings of this study are openly available in Science Data Bank at https://cstr.cn/31253.11.sciencedb.j00186.00829 and https://doi.org/10.57760/sciencedb.j00186.00829.

Declarations

Conflict of interest The authors declare that they have no Conflict of interest.

References

1. M.W. Simon, D. Cline, C.Y. Wu et al. CHICO, a heavy ion detector for Gammasphere. Nucl. Instrum. Methods Phys. Res. Sect. A **452**, 205–222 (2000). https://doi.org/10.1016/s0168-9002(00)00429-0
2. C. Y. Wu, D. Cline, A. Hayes et al., CHICO2, a two-dimensional pixelated parallel-plate avalanche counter. Nucl. Instrum. Methods Phys. Res. Sect. A **814**, 6–11 (2016). https://doi.org/10.1016/j.nima.2016.01.034
3. X.L. Wei, F.H. Guan, H.R. Yang et al., Development of parallel plate avalanche counter for heavy ion collision in radioactive ion beam. Nucl. Eng. Technol. **52**, 575–580 (2020). https://doi.org/10.1016/j.net.2019.08.020
4. S. Y. Xu, Z. Y. Zhang, Z. G. Gan et al., A gas-filled recoil separator, SHANS2, at the China accelerator facility for superheavy elements. Nucl. Instrum. Methods Phys. Res. Sect. A **1050**, 168113 (2023). https://doi.org/10.1016/j.nima.2023.168113
5. K. Yue, Z.Y. Sun, S.T. Wang et al., A CsI (Tl) gamma detection array at the external target hall of CSRm. Nucl. Instrum. Methods Phys. Res. Sect. B **317**, 653–656 (2013). https://doi.org/10.1016/j.nimb.2013.07.037
6. D. Cline, Nuclear shapes studied by Coulomb-excitation. Ann. Rev. Nucl. Part. Sci. **36**, 683–716 (1986). https://doi.org/10.1146/annurev.ns.36.120186.003343
7. M.W. Simon, D. Cline, C.Y. Wu et al., CHICO, a heavy ion detector for gammasphere. Nucl. Instrum. Methods Phys. Res. Sect. A **452**, 205–222 (2000). https://doi.org/10.1016/s0168-9002(00)00429-0
8. T. Poikela, J. Plosila, T. Westerlund et al., Timepix3: a 65k channel hybrid pixel readout chip with simultaneous ToA/ToT and sparse readout. J. Instrum. **9**, C05013 (2014). https://doi.org/10.1088/1748-0221/9/05/c05013
9. C.A. Reidel, C. Schuy, C. Finck et al., Response of the Mimosa-28 pixel sensor to a wide range of ion species and energies. Nucl. Instrum. Methods Phys. Res. Sect. A **1017**, 165807 (2021). https://doi.org/10.1016/j.nima.2021.165807
10. M. Mager, A. Collaboration, ALPIDE, the monolithic active pixel sensor for the ALICE ITS upgrade. Nucl. Instrum. Methods Phys. Res. Sect. A **824**, 434–438 (2016). https://doi.org/10.1016/j.nima.2015.09.057
11. T. Wu, S. Li, W. Wang et al., Beam test of a 180 nm CMOS pixel sensor for the CEPC vertex detector. Nucl. Instrum. Methods Phys. Res. Sect. A **1059**, 168945 (2024). https://doi.org/10.1016/j.nima.2023.168945
12. S. Dong, P. Yang, Y. Zhang et al., Design and characterisation of the JadePix-3 CMOS pixel sensor. Nucl. Instrum. Methods Phys. Res. Sect. A **1048**, 167967 (2023). https://doi.org/10.1016/j.nima.2022.167967
13. M. An, C. Chen, C. Gao et al., A low-noise CMOS pixel direct charge sensor, Topmetal-II¯. Nucl. Instrum. Methods Phys. Res. Sect. A **810**, 144–150 (2016). https://doi.org/10.1016/j.nima.2015.11.153
14. P. Yang, X. Niu, W. Zhou et al., Design of Nupix-A1, a monolithic active pixel sensor for heavy-ion physics. Nucl. Instrum. Methods Phys. Res. Sect. A **1039**, 167019 (2022). https://doi.org/10.1016/j.nima.2022.167019
15. Y. Tian, W. Zhou, Q. Wang et al., A novel silicon pixel sensor for beam monitoringapplications at heavy-ion accelerators. J. Instrum. **19**, C04039 (2024). https://doi.org/10.1088/1748-0221/19/04/c04039
16. K. Akiba, M. Artuso, R. Badman et al., Charged particle tracking with the Timepix ASIC. Nucl. Instrum. Methods Phys. Res. Sect. A **661**, 31–49 (2012). https://doi.org/10.1016/j.nima.2011.09.021
17. R. Ballabriga, J. Alozy, M. Campbell et al., Review of hybrid pixel detector readout ASICs for spectroscopic X-ray imaging. J. Instrum. **11**, P01007 (2016). https://doi.org/10.1088/1748-0221/11/01/p01007
18. J. Adolfsson, A.A. Pabon, M. Bregant et al., SAMPA chip: the new 32 channels ASIC for the ALICE TPC and MCH upgrades. J. Instrum. **12**, C04008 (2017). https://doi.org/10.1088/1748-0221/12/04/c04008
19. F. Anghinolfi, P. Jarron, A.N. Martemiyanov et al., NINO: an ultra-fast and low-power front-end amplifier/discriminator ASIC designed for the multigap resistive plate chamber. Nucl. Instrum. Methods Phys. Res., Sect. A **533**, 183–187 (2004). https://doi.org/10.1016/j.nima.2004.07.024
20. S. Anvar, P. Baron, B. Blank et al., in IEEE Nuclear Science Symposium/Medical Imaging Conference (NSS/MIC)/18th International Workshop on Room-Temperature Semiconductor X-Ray and Gamma-Ray Detectors, Valencia, Spain, 745–749, (2011). https://doi.org/10.1109/NSSMIC.2011.6154095
21. P. Baron, D. Calvet, E. Delagnes et al., AFTER, an ASIC for the readout of the large T2K time projection chambers. IEEE Trans. Nucl. Sci. **55**, 1744–1752 (2008). https://doi.org/10.1109/tns.2008.924067
22. M.D. Rolo, R. Bugalho, F. Goncalves et al., TOFPET ASIC for PET applications. J. Instrum. **8**, C02050 (2013). https://doi.org/10.1088/1748-0221/8/02/c02050
23. M. Ciobanu, N. Herrmann, K.D. Hildenbrand et al., PADI, an ultrafast preamplifier - discriminator ASIC for time-of-flight measurements. IEEE Trans. Nucl. Sci. **61**, 1015–1023 (2014). https://doi.org/10.1109/tns.2014.2305999
24. H.K. Soltveit, J. Stachel, P. Braun-Munzinger et al., The preamplifier shaper for the ALICE TPC detector. Nucl. Instrum. Methods Phys. Res. Sect. A **676**, 106–119 (2012). https://doi.org/10.1016/j.nima.2012.02.012
25. F. Anghinolfi, P. Jarron, F. Krummenacher et al., NINO: an ultra-fast low-power front-end amplifier discriminator for the time-of-flight detector in the ALICE experiment. IEEE Trans. Nucl. Sci. **51**, 1974–1978 (2004). https://doi.org/10.1109/tns.2004.836048
26. F. Zhang, W.X. Peng, K. Gong et al., Design of the readout electronics for the DAMPE silicon tracker detector. Chin. Phys. C **40**, 116101 (2016). https://doi.org/10.1088/1674-1137/40/11/116101
27. C.Q. Feng, D.L. Zhang, S.S. Gao et al., Design of the readout electronics for the Qualification Model of DAMPE BGO calorimeter. in 19th IEEE-NPSS Real Time Conference, Nara, Japan, 1–1 (2014). https://doi.org/10.1109/RTC.2014.7097466
28. V. Stankova, J. Barrio, J.E. Gillam et al., Multichannel DAQ system for SiPM matrices.2012 IEEE Nuclear Science Symposium and Medical Imaging Conference Record (NSS/MIC), Anaheim, CA. USA **1069–1071**, 2012 (2012). https://doi.org/10.1109/NSSMIC.2012.6551270
29. A. Francesco, R. Bugalho, L. Oliveira et al., TOFPET 2: a high-performance circuit for PET time-of-flight. Nucl. Instrum. Methods Phys. Res. Sect. A **824**, 194–195 (2016). https://doi.org/10.1016/j.nima.2015.11.036

30. D.-X. Wang, C.-J. Lin, L. Yang et al., Compact 16-channel integrated charge-sensitive preamplifier module for silicon strip detectors. Nucl. Sci. Tech. **31**, 48 (2020). https://doi.org/10.1007/s41365-020-00755-0
31. Z. Chen, C. Feng, H. Chen et al., Readout system for a prototype multi-purpose time projection chamber at CSNS Back-n. J. Instrum. **17**, P05032 (2022). https://doi.org/10.1088/1748-0221/17/05/p05032
32. V. Álvarez, F.I.G.M. Borges, S. Cárcel et al., NEXT-100 technical design report (TDR) - executive summary. J. Instrum. **7**, T06001 (2012). https://doi.org/10.1088/1748-0221/7/06/T06001
33. J. Rodriguez, J. Toledo, R. Esteve et al., The front-end electronics for the 1.8-kchannel SiPM tracking plane in the NEW detector. J. Instrum. **10**, C01025 (2015). https://doi.org/10.1088/1748-0221/10/01/c01025
34. K. Hu, W. Li, Y. Li et al., Improvement of sigma delta charge readout method for radiation detector application. Nucl. Instrum. Methods Phys. Res. Sect. A **1024**, 166054 (2022). https://doi.org/10.1016/j.nima.2021.166054
35. M. Zhao, C. Feng, Z. Zhou et al., Low noise front-end electronics for a CZT-based gamma-ray spectrometer. IEEE Nuclear Science Symposium and Medical Imaging Conference (NSS/MIC), Piscataway, NJ. USA **1–5**, 2021 (2021). https://doi.org/10.1109/NSS/MIC44867.2021.9875590
36. B. Zhang, X. Wei, S. Zhang et al., Design and simulation for pre-amplifier of ITER radial X-ray camera. J. Fusion Energy **37**, 136–143 (2018). https://doi.org/10.1007/s10894-018-0160-7
37. M. Nakhostin, M. Baba, Pulse-shape discrimination of alpha particles of different specific energy-loss with parallel-plate avalanche counters. IEEE Trans. Nucl. Sci. **61**, 1326–1332 (2014). https://doi.org/10.1109/tns.2014.2322571
38. M. Cortesi, Y. Ayyad, J. Yurkon, Development of a parallel-plate avalanche counter with optical readout (O-PPAC). J. Instrum. **13**, P10006 (2018). https://doi.org/10.1088/1748-0221/13/10/p10006
39. H. Kumagai, T. Ohnishi, N. Fukuda et al., Development of parallel plate avalanche counter (PPAC) for BigRIPS fragment separator. Nucl. Instrum. Methods Phys. Res. Sect. B **317**, 717–727 (2013). https://doi.org/10.1016/j.nimb.2013.08.050
40. S. Di Carlo, M. Cortesi, Parallel-plate avalanche counters for heavy-ion beam tracking: history and mysteries. Phys. Rev. Accel. Beams **27**, 044801 (2024). https://doi.org/10.1103/PhysRevAccelBeams.27.044801
41. A. Jhingan, H.J. Wollersheim, R. Kumar et al., An annular parallel plate avalanche counter for heavy-ion γ-ray coincidence measurements. Nucl. Instrum. Methods Phys. Res. Sect. A **922**, 209–216 (2019). https://doi.org/10.1016/j.nima.2018.12.075
42. OPA657, https://www.ti.com/product/OPA657. Accessed 22 Jan 2025
43. OPA847, https://www.ti.com/product/OPA847. Accessed 22 Jan 2025
44. Rohde & Schwarz HMP4040 regulated power supply, https://www.rohde-schwarz.com/us/products/test-and-measurement/dc-power-supplies/rs-hmp4000-power-supply-series$_$63493-47360.html. Accessed 29 Apr 2025
45. Fluke iSee Mobile Thermal Camera - TC01A, https://www.fluke.com/en-us/product/thermal-cameras/fluke-tc01a-tc01b. Accessed 29 Apr 2025
46. Tektronix AFG 31252 signal generator, https://www.tek.com/en/datasheet/arbitrary-function-generators. Accessed 29 Apr 2025
47. Rohde & Schwarz MXO44 oscilloscope, https://www.rohde-schwarz.com/us/products/test-and-measurement/oscilloscopes/rs-mxo-4-oscilloscope_63493-1164992.html. Accessed 29 Apr 2025
48. Keysight InfiniiVision MSOX6004A oscilloscope, https://www.keysight.com/us/en/product/MSOX6004A/mixed-signal-oscilloscope-1ghz-6ghz-4-analog-16-digital-channels.html. Accessed 29 Apr 2025
49. Tektronix DPO5034B oscilloscope, https://www.tek.com/en/datasheet/mixed-signal-oscilloscopes. Accessed 29 Apr 2025
50. FTA820A Octal Fast Timing Amplifier, https://www.ortec-online.com/products/electronic-instruments/amplifiers/fta820a. Accessed 29 Apr 2025
51. CF8000 octal constant-fraction discriminator, https://www.ortec-online.com/products/electronic-instruments/fast-timing-discriminators/cf8000. Accessed 22 Jan 2025
52. V775 - 32 channel multievent TDC (35÷300 ps), https://www.caen.it/products/v775/. Accessed 22 Jan 2025
53. Geant4, https://geant4.web.cern.ch/. Accessed 29 Apr 2025